Chambers, J E, Loke, M H, Ogilvy, R D, and Meldrum, P I, 2004. Non-invasive monitoring of DNAPL migration through a saturated porous medium using electrical impedance tomography. Journal of Contaminant Hydrology.Vol. 68, 1-22.

NON-INVASIVE MONITORING OF DNAPL MIGRATION THROUGH A SATURATED POROUS MEDIUM USING ELECTRICAL IMPEDANCE TOMOGRAPHY

Chambers, J E[1*], Loke, M H[2], Ogilvy, R D[1] and Meldrum, P I[1]
[1]British Geological Survey, Keyworth, Nottingham, NG12 5GG, UK.
[2]School of Physics, Universiti Sains Malaysia, 11800 Penang, Malaysia.

ABSTRACT

Electrical impedance tomography was used to monitor the movement of a fluorinated hydrocarbon DNAPL through a saturated porous medium within a laboratory column. Impedance measurements were made using a horizontal plane of twelve electrodes positioned at regular intervals around the centre of the column. A 2D inversion algorithm, which incorporated the cylindrical geometry of the column, was used to reconstruct resistivity and phase images from the measured data. Differential time-lapse images of DNAPL movement past the plane of electrodes were generated by the cell-by-cell subtraction of resistivity and phase baseline models from those associated with the DNAPL release stage of the experiment.

The DNAPL pulse was clearly delineated as resistive anomalies in the differential time-lapse resistivity images. The spatial extent of the resistive anomalies indicated that, in addition to vertical migration, some lateral spreading of the DNAPL had occurred. Residual contamination could be detected after quasi-static conditions were re-established. Residual DNAPL saturation was estimated from the resistivity model data by applying Archie's second equation.

Despite significant measured phase changes due to DNAPL contamination, the differential phase images revealed only weak anomalies associated with DNAPL flow; these anomalies could be seen only in the initial stages of the experiment during peak flow through the plane of electrodes.

KEY WORDS

DNAPLs; impedance; tomography; laboratory column; monitoring; geophysics

[*] Corresponding author. British Geological Survey, Keyworth, Nottingham, NG12 5GG, UK. Fax: +44(0)115 936 3261
Email address: Jonathan.Chambers@bgs.ac.uk

1. INTRODUCTION

Groundwater contamination by dense nonaqueous phase liquids (DNAPLs), such as chlorinated solvents, PCB oils and creosotes, has been increasingly recognised as a serious environmental problem. DNAPLs have been widely used by a range of industries for many decades, and have been introduced into the subsurface by spills, uncontrolled releases and leaking storage and disposal facilities (Rivett et al., 1990; Pankow et al., 1996). Upon release DNAPLs spread under the influence of gravity until they are distributed to such an extent that residual levels are attained and capillary trapping prevents further movement, or an impermeable layer is reached, at which point pooling and lateral spreading may occur (Schwille, 1988; Mercer and Cohen, 1990; Pankow and Cherry, 1996). DNAPLs are typically characterised by low solubilities and are resistant to biodegradation and natural attenuation (Lucius et al., 1992; Pankow et al. 1996); they are, however, soluble enough to cause levels of contamination far greater than those permissible in drinking water. Consequently, even small amounts of DNAPL can present a long-term source of contamination (Johnson and Pankow, 1992).

The characterisation of DNAPL contaminated sites and source zones are essential for the successful design of remedial strategies (Cohen and Mercer, 1993; Feenstra and Cherry, 1996; Gavaskar et al., 2000). Conventional site investigation relies in part upon intrusive methods, such as boreholes and cone penetration tests. These techniques provide limited spatial information of the subsurface at discrete intervals, and have the potential to spread contamination by opening DNAPL migration pathways through low permeability zones (Feenstra and Cherry, 1996; Broholm et al. 1999). Alongside intrusive techniques geophysical methods are now beginning to be applied to DNAPL contamination problems (ITRC, 2000), both to assist in site characterisation (e.g. Chambers et al., 1999) and to monitor remedial processes (e.g. Daily and Ramirez, 1995; Newmark et al., 1998). Geophysical techniques can have the advantages of reducing the need for intrusive investigations, and can provide spatially continuous information regarding subsurface structure (Reynolds, 1997).

The technique considered in this study is electrical impedance tomography (EIT). Electrical impedance measurements carried out by Olhoeft (1985) and Vanhala (1997) on laboratory samples have indicated that NAPL contaminated materials may be discriminated on the basis of altered electrical properties. This research has provided the basis for the use of EIT as a means of detecting and monitoring DNAPL contamination (Weller et al., 1996b; Daily et al., 1998).

The aim of this study is to demonstrate the effectiveness of EIT as a means of detecting and monitoring DNAPL distribution within a water-saturated porous medium. An experiment is described in which a DNAPL is released within a laboratory column and is monitored using time-lapse EIT.

2. ELECTRICAL IMPEDANCE TOMOGRAPHY

Electrical impedance is a complex quantity consisting of a magnitude and a phase component. Impedance magnitude is the amplitude of the frequency dependent resistance, whilst the impedance phase is a measure of induced polarization (IP). Measurements can be made over a range of frequencies so that the frequency dependence of the materials of interest may be assessed; this method is termed spectral induced polarization (SIP) or complex resistivity.

The two main mechanisms of IP are membrane and metallic polarization (Sumner, 1976). Membrane polarization occurs when the movement of ions within a rock mass is restricted, due to blockages at pore throats caused by layers of loosely bound ions on the mineral grain surfaces. As an electrical current is applied, concentrations of ions build up around these blockages causing membrane polarization. When the current is removed the ions migrate back to their original positions, thereby generating a transient decay voltage. Membrane polarization is particularly associated with the presence of clay minerals. Metallic polarization occurs when a voltage is applied across an electrolyte filled pore space blocked by a conducting mineral grain. The transfer from electrolytic conductance to electrical conductance impedes the current flow, and the

electrolyte/mineral interface becomes polarized. As applied voltage is removed a transient decay voltage is produced as the ions diffuse back to their original positions. Marshall and Madden (1959) indicate that membrane and metallic polarization effects are difficult to distinguish on the basis of their electrical behaviour, as they both result from diffusion processes. Other mechanisms of IP have been identified, including electrokinetic, thermoelectric and electromagnetic effects (Marshall and Madden, 1959) and clay-organic reactions (Olhoeft, 1985).

EIT involves the collection of data sets comprising multiple electrical measurements (amplitude and phase). This requires the use of computer controlled automated measurement systems and multi-electrode arrays, due to the typically large number of measurements made during the course of a survey. Numerical inversion of these data is undertaken to produce tomograms of subsurface electrical property distributions. Examples of electrical impedance imaging procedures are given by Cho (1996), Ramirez et al. (1999), Daily et al. (2000) and Kemna et al. (2000).

3. EXPERIMENTAL PROCEDURE

3.1 Experimental Design

The laboratory column (Figure 1) measured 520 mm in height, with an internal diameter of 310 mm. The base of the column was sealed with a plastic plate. An in/outflow valve was positioned at the base of the column to allow saturation and drainage of the column. The column was constructed using PVC; silicone rubber was used as a sealant and adhesive. Twelve 10 mm diameter carbon electrodes were positioned at regular intervals around the centre of the column at a height of 260 mm. The flat ends of the electrodes were flush with the internal column wall.

The column was filled with a range of porous materials, as shown in Figure 1. A coarse washed silica sand layer (BS Mesh 16/30), 40 mm thick, was positioned at the base of the column. A ring of fine washed silica sand (AFS 95), 20 mm thick, was introduced around the sides of the column. This ring was intended to act as a capillary barrier to the DNAPL, thereby preventing the coating of

the electrodes by the organic liquid. The central area of the column was filled with a polarizable medium that comprised an 80:20 dry weight percent mix of coarse sand and iron grit. A medium grained (BS Mesh 22/52) iron grit was used, comprising angular grains varying in size from 0.3 to 0.71 mm. The sand and iron grit were thoroughly mixed and placed carefully into the column, with further in-situ mixing, to minimise heterogeneities arising from the localised sorting of grains. Though a perfectly homogeneous mix was not achievable, it was anticipated that mixing was sufficient to minimise disruption of DNAPL flow on a macroscopic scale. The column was saturated with tap water (~ 17 Ωm) from the base of the column.

Iron grit was used in the place of clay to provide a relatively permeable polarizable medium. Sand-clay mixes displaying a suitably high IP effect (>10 mrads) were found to be essentially impermeable to DNAPL over the timescale of a few days, due to the blocking of pores by clay grains. It was anticipated from prior testing of contaminated samples that the scale of DNAPL induced phase changes would be of a similar order to that observed with the organic contamination of clay containing samples (Vanhala, 1997), and would therefore allow the potential for EIT to detect phase changes of this magnitude to be assessed.

A hydrocarbon DNAPL, 3M™ Novec™ HFE-7200 engineered fluid, used here as a surrogate for other more toxic industrial DNAPLs, was introduced into the column through a 25 mm diameter polycarbonate tube embedded approximately 80 mm into the sand. A head of approximately 80 mm, equivalent to a capillary pressure of ~1122 Nm^{-2}, was maintained during the DNAPL release phase in order to overcome the entry pressure of the sand. The minimum pore diameter invaded by DNAPL is given as (Kueper and McWhorter, 1991),

$$e = \frac{4\sigma \cos\theta}{P_e} \qquad (1)$$

where, e is the pore throat diameter, σ is the interfacial tension between NAPL and water, θ is the contact angle at the solid-fluid-fluid interface, and P_e is the entry pressure. Given an entry pressure

of 1122 Nm^{-2} and the fluid properties in Table 1, it was calculated, using equation (1), that pore throats with diameter of greater than 118 μm would be invaded at the porous medium-DNAPL interface. With increasing depth in the column, capillary pressure was expected to increase (Kueper and McWhorter, 1991), resulting in the invasion by DNAPL of pore throats with diameters of less than 118 μm. Water displaced by the DNAPL overflowed and was collected from the top of the column.

Novec™ HFE-7200 is a practically non-toxic and non-flammable colourless fluorinated liquid with a number of physical properties (Table 1) similar to those of trichloroethene (TCE), which is one of the most commonly occurring industrial DNAPL contaminants (Pankow et al., 1996). It has a high chemical stability and appears not to react with the materials comprising the column and the infilling sand and iron. Furthermore, the low solubility (Table 1), volatility and evaporation rate of HFE-7200 will result in minimal mass loss of DNAPL from the system during the course of the experiment. HFE-7200 is an extremely difficult liquid to dye, and at the time of this study a suitable dye was not available; visual confirmation of the NAPL flow pathway after the infiltration experiment could not be achieved. Studies by Schwille (1988), Kueper et al. (1989) and Oostrom et al. (1999) do however indicate that in a saturated homogeneous coarse-grained porous medium DNAPL would be expected to migrate downwards through the column with limited lateral spreading, either as a front or as fingers. In this case, given the density (d) and viscosity (μ) of the DNAPL used, i.e. $d_{\mathrm{DNAPL}} > d_{\mathrm{water}}$, $\mu_{\mathrm{DNAPL}} < \mu_{\mathrm{water}}$, it is likely that unstable flow and fingering will have occurred (Trantham and Durnford, 1999).

3.2 Data Collection

Instrumentation

A multichannel complex resistivity system (Radic-Research SIP256b) was used for data acquisition. The system comprised a base unit housing a current source and signal generator, twelve remote

units each containing a 24 bit A/D converter, and a computer to control the system and archive the data. Each measurement electrode was attached to the system through a remote unit. A schematic diagram of the system is shown in Figure 2a. The computer interface allowed the input current and measured amplitude and phase to be monitored during the data collection process.

The system was operated using predefined measurement protocols that were read by the control program. For each measurement position, electrodes were selected as either current sources or used for potential measurements; each electrode pair not used as current sources were automatically employed to measure potential. The array configuration used during this study is summarised in Figure 2b. A full scan comprised twelve measurement positions, in which all possible combinations of the dipole-dipole array, for which the current and potential dipole lengths equalled one unit electrode separation, were utilised. A single frequency scan carried out using this measurement protocol comprised 108 measurement points, which consisted of 54 normal and 54 reciprocal measurements. A single measurement at a frequency of 5 Hz comprised an input current pulse duration of 4 seconds, with a further 18.5 seconds required for data processing. Each twelve-measurement scan took 270 seconds. Movement of DNAPL during individual scans will inevitably have led to the blurring and averaging of model resistivity values, particularly during the most dynamic phase of DNAPL infiltration. Consequently, peak model resistivity values may underestimate the true formation resistivity.

SIP measurements made on a sample of the sand/iron mix used in this experiment, at frequencies of between 0.6 and 125 Hz, indicated a phase peak situated between 5 and 10 Hz. Testing also revealed that contamination of the material with HFE-7200 resulted in a reduction in the phase peak, with the greatest reduction in phase occurring between 5 and 10 Hz. In order to ensure that the maximum phase contrast between contaminated and uncontaminated material could be achieved, measurements were made using a 5 Hz injection current. A frequency of 5 Hz also represented a good compromise between the faster measurement rates and poorer data quality associated with

higher frequency measurements, and the much slower measurement rates but higher data quality associated with measurements made at lower frequencies (Ramirez et al., 1999).

Measurement Error

Measured data is subject to error from a variety of sources, including that introduced by the measurement device, poor electrode contact or electrode polarization, and other indeterminate external effects (Sumner, 1976). Comparison of normal and reciprocal data points has been identified in other studies as a good measure of data quality (Binley et al., 1996; Ramirez et al. 1999). In this study reciprocal error was calculated as the percentage difference between normal and reciprocal data points, unless otherwise stated. An additional measure of error used in this study was that calculated by the SIP256b system in the frequency domain from time series measured for voltage and for current; the method is the same as that used in magnetotellurics (Bendat and Piersol, 1971). A relative error is calculated for magnitude and an absolute error is given for phase.

Prior to data collection a test was carried out using a blank tap water sample; the water represented a non-polarizable target and was expected to produce a phase response of zero. Reciprocal errors for the measured amplitude data were typically less than 1%, whilst measured phase shift were predominantly less than ± 1 mrad. These results indicated that measurement errors associated with the instrument and column were low, and that the carbon electrodes used in the experiment had only a very small polarizability. Reciprocal errors from the amplitude and phase data collected during the DNAPL infiltration experiment described in this study were predominantly below 2 and 10%, respectively. Calculated errors from the SIP256b system for the magnitude data at 5 Hz were typically less than 1%; likewise, errors calculated for phase were small, predominantly less than 2 mrads. Normal measurements were used as default. However, measurements with a reciprocal error of greater than 5% were reassessed on the basis of calculated error, and the point with the lowest calculated error was used, whether normal or reciprocal.

Measurement Procedure

Prior to DNAPL release a scan was carried out in order to characterise the static water saturated conditions within the column, and to provide baseline sections with which to produce differential time-lapse images from subsequent scans. Upon the release of the DNAPL, continuous scans were made for a period of 3.5 h, after which time pairs of scans were collected at approximately 30 min intervals. The DNAPL drained entirely from the surface of the column within 30 min. Measurements were stopped 8.5 h after the initial release of the DNAPL.

4. NUMERICAL INVERSION

In order to interpret the data from this experiment, a finite element (Silvester and Ferrari, 1990) forward modelling subroutine to calculate the electrical response of a cylindrical structure due to point current sources was used. To simplify the computations needed, it was assumed that the column has a cylindrical shape that extends to infinity at both ends, i.e. a 2D structure. By reducing the problem to a 2D geometry, the computer time required for the finite-element subroutine can be significantly reduced. Only a brief outline of the finite-element method is given here as the details can be found in other sources (Coggon, 1971; Sasaki, 1989). The DC response of a 2D structure is given by Poisson's equation,

$$-\frac{1}{\rho(x, z)}\nabla^2\phi(x, y, z) = I_S(x, y, z) \qquad (2)$$

where $\rho(x, z)$ is the resistivity distribution, and $\phi(x, y, z)$ is the electrical potential due to a source current distribution $I_S(x, y, z)$. While the structure is 2D, the potential distribution and current source is 3D. To reduce the 3D equation to a series of 2D equations, a Fourier transform of equation (2) in the *y*-direction is carried out, which results in the following 2D partial differential equation

$$-\left[\nabla.\left(\frac{1}{\rho(x, z)}\nabla\Phi(x, \lambda, z)\right) - \frac{\lambda^2}{\rho(x, z)}\Phi(x, \lambda, z)\right] = -\tilde{I}_s(x, \lambda, z) \qquad (3)$$

where λ is the Fourier transform variable. The finite element discretisation of the above equation results in a matrix equation

$$\mathbf{C}\,\mathbf{\Phi} = \mathbf{I} \tag{4}$$

where **C** is the capacitance matrix that contains the geometry and resistivity of the mesh elements. It is a symmetric, sparse and banded matrix. The matrix equation is usually solved using a direct method such as the sparse Cholesky method (George and Liu, 1981) for 2D problems. The solution of the matrix equation in (4) gives the transformed potential, $\Phi(x,\lambda,z)$ in the (x,λ,z) space for a range of λ values (Weller et al., 1996a). To obtain the potential in the (x,y,z) space, the following inverse Fourier transform is carried out by numerical integration.

$$\phi\,(x,0,z) = \frac{1}{\pi}\int_0^{\infty} \Phi\,(x,\lambda,z)\,d\lambda \tag{5}$$

To accurately simulate the curved surface of the cylinder, an isoparametric quadrilateral element with 8 nodes is used (Figure 3a). The arrangement of cells in concentric rings (Figure 3a) was chosen so that adjacent sides in any quadrilateral element are almost orthogonal. This results in a more stable numerical system of equations and consequently greater accuracy in the calculated potentials (Silvester and Ferrari, 1990). This arrangement avoids cells with almost colinear adjacent sides that are numerically less stable. Within the element, the potential is approximated by a quadratic function. By applying an isoparametric transformation on the quadrilateral element, the nodes on each cell can be shifted such that they coincide with corresponding points on the cylindrical cells. Each side of the quadrilateral element follows a quadratic curve. If the elements are sufficiently small, the curved surface of the cylinder can be accurately modelled by such curved elements. Two quadratic elements are placed between adjacent electrodes in the forward modelling subroutine (Figure 3a). Tests using four elements between adjacent electrodes did not show significant changes in the calculated potential values. To minimise any errors due to mismatch between the true shape of the cylinder and the quadratic elements, the electrodes are placed at the

middle node on the side of the element (node 2 in Figure 3a). Note that the centre of the cylindrical model is a point. Triangular elements were used to model the central core of the cylinder.

Ends effects due to the finite length of the column were minimised by placing the electrodes at the centre of the column. Experiments with a homogeneous material (tap water) filling the column showed that end effects are not significant. Table 2 shows the results from measurements made with the dipole-dipole array with the 'n' factor ranging from 1 to 5. The geometric factors were determined empirically by calculating the resistance values measured by the same array configuration for a homogeneous cylindrical body with the same radius using the finite-element forward modelling program. The geometric factor is given by the ratio of the calculated resistance value and the resistivity of the synthetic model. The empirical geometric factors were compared with analytical values given by Weidelt and Weller (1997). The average difference between the empirical and analytical geometric factors was 2.3% with a maximum difference of 4.8%. The difference is probably partly due to the finite length of the cylinder that is not taken into account in the 2D finite-element program. One possible advantage of the finite-element approach in calculating the geometric factors is that it can be extended for bodies with a non-cylindrical geometry, such as tree trunks (Hagrey et al., 2003). The apparent resistivity values in Table 2 show a small but systematic increase of about 5% as the dipole-dipole 'n' factor increases from 2 to 5. However, even measurements with the same 'n' value show some variation due to asymmetries in the experimental design; such as the variations in the distances between adjacent electrodes, departures from a perfect cylinder and variations in the fine sand layer next to the electrodes. It is expected that the change in the measured resistance values due to the finite ends of the cylinder should be similar for different sets of measurements. While this will influence the inversion model from a single set of measurements, it should have minimal effect on the differential resistivity images.

Apparent IP (chargeability) values were calculated by using the following formula (Oldenburg and Li, 1994)

$$\eta_a = \frac{\phi_\eta - \phi_\rho}{\phi_\eta} \quad (6)$$

where ϕ_ρ is the DC resistivity potential while ϕ_η is the potential for a modified resistivity distribution ρ_η. The modified resistivity distribution is given by

$$\rho_\eta(x, y, z) = \frac{\rho_{DC}(x, y, z)}{1 - \eta(x, y, z)} \quad (7)$$

where $\eta(x, y, z)$ is the model chargeability distribution. The chargeability values in mV/V can be converted into phase angles, and vice versa, using the relationships given in Van Voorhis et al. (1973) and Nelson and Van Voorhis (1973).

The measured data consist of the apparent resistivity and phase measurements with different sets of electrodes. The purpose of the data inversion is to convert these measurements into the resistivity and IP values in different parts of the cylindrical cross-section. The smoothness-constrained Gauss-Newton least-squares optimisation method that is commonly used for the inversion of data from 2D electrical surveys along the ground surface (Oldenburg and Li, 1994; Loke and Dahlin, 2002) was adapted for this study. This method uses the following equation

$$(\mathbf{J_i^T J_i} + \boldsymbol{\lambda_i} \mathbf{C^T C}) \boldsymbol{\Delta p_i} = \mathbf{J_i^T g_i} - \boldsymbol{\lambda_i} \mathbf{C^T C p_i} \quad (8)$$

where $\boldsymbol{\Delta p_i}$ is the model parameters (the logarithm of the resistivity) change vector for the *i*th iteration, **J** is the Jacobian matrix of partial derivatives and **g** is the data misfit vector (Lines and Treitel, 1984). A first order finite-difference operator (deGroot-Hedlin and Constable, 1990) was used for the roughness filter **C**. A two step process was used for the inversion of the resistivity and IP data. Firstly the inversion of the apparent resistivity data was carried out to obtain a resistivity model. This resistivity model was then used as a background resistivity model in the inversion of the apparent phase data to construct an IP model (Oldenburg and Li, 1994). The discretised

inversion model, consisting of a number of concentric circular zones that were subdivided into a number of cells, is shown in Figure 3a; the resulting model has 7 zones and 168 cells.

Equation (8) minimises the sum-of-squares (a l_2 norm) of the change in the model resistivity values (the $\mathbf{C}^T\mathbf{C}$ term) between adjacent cells. The resistivity variations within such a model will have smooth boundaries. Since it is expected that the DNAPL will spread gradually as it flows down the column, this constraint is close to the actual situation. However, the use of such a smoothness constraint will result in poorer resolution in areas with sharp boundaries (Loke and Lane, 2002) such as the interface between the fine silica sand ring around the sides of the column and inner coarse sand/iron mix. A modified least-squares optimisation method using the l_1 norm, commonly referred to as a blocky inversion method (Ellis and Oldenburg, 1994; Loke and Lane, 2002) that produces an inversion model with sharper boundaries, is also available in the computer program used.

Some smearing of the images may occur due to the finite time required for each measurement as well as the assumption of a 2D geometry. Since changes in the resistivity variations will occur during the time required for each set of measurements, the inversion model probably gives an 'average' of the true resistivity during the measurement time. The resistivity distribution also changes along the length of the column. Each 2D image is also affected by the resistivity of the material above and below the ring of electrodes. However, since lateral spreading of the DNAPL is likely to be much slower than the rate of flow down the column, such 3D effects are probably not significant.

One possible disadvantage of the model discretisation used in Figure 3a is that the cells become progressively narrower towards the centre of the cylinder. In order to verify that the model discretisation and regularisation method chosen does not result in significant artefacts in the inversion models, two series of tests with structures of known geometry were carried out. The first series used synthetic data generated using the finite-element forward modelling program. In the second set of tests, measurements were made with the cylinder filled with water and objects such as

plastic tubes or metal rods placed within the cylinder. Both sets of tests confirmed that the inversion results are not significantly influenced by the model discretisation and regularisation method used. As an example, Figure 3b shows the results from a test where a plastic tube was used. The inversion model shows a high resistivity anomaly in the region of the tube without significant artefacts in other parts of the cylinder.

5. RESULTS AND DISCUSSION

5.1 Baseline Models

The baseline resistivity and phase scans are shown as Figure 4. Model resistivities of the coarse sand/iron mix are seen to vary between 50 and 60 Ωm, whilst the fine sand around the edge of the column is associated with resistivities of approximately 70 Ωm. The phase model indicates that the sand/iron mix had a phase response as high as 160 mrads. A zone of relatively low phase values is seen around the edge of the model reflecting the presence of the fine sand. The phase values shown in the model for this zone are still much higher than would be expected for clean sand, indicating imperfect resolution of the fine sand layer. Thin layers of greatly contrasting electrical properties are, however, typically difficult to precisely resolve using smoothness constrained inversion methodologies (Chambers, 2001). Both the resistivity and phase models contained heterogeneities, in particular resistivity and phase lows were observed towards the centre of the models. These heterogeneities are likely to be a function of the mixing of the sand and iron, and possibly artefacts of electrode array and FE mesh geometry. The use of differential imaging was intended to reduce the effects of these heterogeneities by allowing the changes in electrical properties produced by the presence of DNAPL to be considered in isolation.

5.2 Measured Breakthrough Curves

Prior to the inversion of the tomographic data, measured data were extracted for a dipole-dipole configuration comprising remote units 7 (C1) and 8 (C2), and 10 (P1) and 11 (P2); these measured data were used to provide an indication of DNAPL movement past the plane of electrodes. This electrode configuration was chosen due to its close proximity to the lateral position of the DNAPL release point. Figure 5 shows measured amplitude and phase data collected from this electrode configuration between t = 0 and 213 min. The measured amplitude can be seen to increase with the introduction of the highly resistive DNAPL. A rapid increase in amplitude can be seen to occur between t = 0 and 25 min, before an equally rapid decline from t = 25 to 50 min. After this point the change in amplitude was minimal indicating a return to essentially static conditions. The measured phase angle curve mirrored that of the amplitude; phase angles were shown to markedly drop with the introduction of DNAPL. This may have been due to DNAPL enveloping the metallic grains, thereby preventing metallic polarization from occurring. These curves indicate that the DNAPL migrated rapidly through the column with peak flow of DNAPL past the electrodes occurring within 30 min of DNAPL release; a majority of DNAPL movement appears to have occurred with the first hour of the experiment. Both the measured amplitude and phase curves showed an offset at t = 213 min from original levels at t = 0, due almost certainly to the presence of residual DNAPL.

5.3 Time Lapse Imaging

The differential time-lapse resistivity and phase images of DNAPL induced changes between t = 4.5 and 481.5 min are shown in Figure 6. Differential images were produced by the cell-by-cell subtraction of baseline model from subsequent models. It should be noted that small-scale intergranular features, such as fingers and isolated blobs (Schwille, 1988), are beyond the resolution of the electrical imaging configuration used in this case; DNAPL contaminated zones will be distinguished as laterally continuous resistivity or phase anomalies with each model cell indicating an average resistivity or phase value for the area of the cell.

The resistivity images show a marked resistive anomaly coinciding with the lateral position of the DNAPL release point. This anomaly can be seen to intensify up to t = 22.5 min before diminishing, with a peak corresponding with that of the measured data curves (Figure 5). These anomalies clearly reflect the migration of the DNAPL past the plane of electrodes. As anticipated, the size of the anomalies relative to the release point diameter indicates some lateral spreading of the DNAPL with downward migration. Maximum increases in resistivity associated with the presence of DNAPL are approximately 35 Ωm, seen at t = 22.5 min. As previously mentioned these model resistivity changes may represent an underestimate of true peak resistivities. However, model resistivity increases (~35 Ωm) are small enough to indicate that full DNAPL saturation within the migration pathway within the plane of electrodes probably did not occur; instead it is probable that, due to variability in pore throat diameter (equation (1)) and fingering, some pore spaces within the main DNAPL pulse remained wholly or partially water filled thereby permitting electrolytic conduction through the main zone of contamination.

The phase images are very much more heterogeneous and variable, reflecting the greater sensitivity of phase measurements to noise. At t = 13.5 and 22.5 min, over the same time as the peak in resistivity occurred (Figure 6), small phase lows can be seen below the DNAPL release point, most likely indicating the presence of DNAPL. No other features within the phase images shown in Figure 6 can be linked with any confidence to the presence of DNAPL, despite measured phase shifts of up to 14 mrads. These phase shifts are of a similar order of magnitude to those reported by Vanhala (1997) for oil contaminated glacial till and sand samples. Though the IP mechanisms identified by Vanhala (1997) were different to those operating during this study, i.e. clay-organic reactions or disrupted membrane polarization, the implications for the ability of EIT to image phase changes of this magnitude are the same. Detection of these levels of DNAPL induced phase shifts in the field environment, where there are fewer controls and greater noise influences, is likely to be even more problematic.

5.4 Model Breakthrough Curves

Slater et al. (2000) describe an experiment in which time-lapse resistivity model cells were used to produce multiple breakthrough curves describing the movement of a saline tracer through a porous medium. In this study a similar procedure is used to monitor DNAPL migration. Figure 7 shows model resistivity and phase breakthrough curves for cells 38 and 142. Cell 38 is located directly below the DNAPL release point, and consequently coincides with the modelled DNAPL flow path (Figure 6); cell 142 is situated on the opposite side of the column.

The model breakthrough curves for the phase are highly variable, probably as a result of noise, and systematic variation corresponding to DNAPL movement is difficult to detect. The cell 38 curve does however display a phase low, consisting of three points, at t = 13.5 to 22.5 min corresponding to the rise to peak DNAPL saturation within the plane of electrodes. Conversely, the resistivity breakthrough curves are relatively smooth, with few irregular datum points. Cell 142 shows only slight changes in model resistivity, with a maximum change of <5 Ωm. After 3.5 h an offset of <3 Ωm from the starting resistivity is observed. It is likely that the slight variation in amplitude is related to resistivity changes in other parts of the column, and is a result of the smoothing inherent in the inversion routine. The cell 38 curves display a similar pattern to that seen from the measured amplitude curve in Figure 5. A steady increase in resistivity up to 87 Ωm is seen within 22.5 min of DNAPL release. A rapid decline is then seen corresponding to the passing of the DNAPL before virtually static conditions are reached after approximately 60 min. After 3.5 h little change in resistivity is seen, with values holding steady at around 69 Ωm, representing an offset of 15 Ωm from the starting resistivity.

5.5 Estimation of DNAPL Saturation

DNAPL saturation was estimated using the second Archie equation (Archie, 1942)

$$S_w = \left(\rho_o / \rho_t \right)^{1/n} \quad (9)$$

where S_w is the fraction of pores containing water, ρ_o is the resistivity of the water-saturated sediment, ρ_t is resistivity of partially saturated sediment, and n is the saturation exponent, usually 2. This equation was originally developed to determine reservoir characteristics of oil and gas bearing formations, though latterly it has also been applied to environmental problems (e.g. Daily et al., 1992; Schima et al., 1996; Weller et al., 1996b). The Archie equation is typically applied to clean materials with no conductive matrix components. The presence of conductive matrix components can lead to an overestimation of S_w, particularly at low water saturations (Hearst et al., 1999). However, in this case the iron component, approximately 4.5% by volume, is expected to have only a modest effect on the calculated saturations as the grains are disseminated, preventing metallic electrical continuity (Clavier et al., 1976). Consequently, it is assumed that the Archie equation will provide an approximate indication of the DNAPL saturation, particularly at the high water saturations (e.g. S_w > 75%) associated with residual DNAPL levels. For a clean water-saturated porous medium with a resistivity of 54 Ωm, reflecting the value of cell 38 at t = 0, Table 3 shows how resistivity changes with increasing DNAPL saturation, according to equation (9). DNAPL saturations calculated for cell 38 between t = 0 and 213 min are shown on Figure 7. The curve shows maximum DNAPL saturations of 21% of pore space, reducing to approximately 12% with time. The maximum saturation level is subject to increased uncertainty due to the likely underestimation of peak resistivity values. Saturation levels calculated during less dynamic periods of the experiment, i.e. after t = 60 min are less likely to be affected by these averaging and smoothing effects.

Figure 8 shows a contour plot of inferred DNAPL residual saturations across the column at t = 8.5 h; residual saturation levels were calculated for each cell using the equation above. The plot shows residual DNAPL saturation values of up to 12% directly below the DNAPL release point within the zone identified in Figure 6 as the DNAPL migration pathway. These values are towards the lower

end of those recorded by other researchers. Imhoff et al. (1998) recorded average residual TCE saturations of 12 and 13% from saturated medium grained glass beads and sand, respectively. Cohen and Mercer (1993) list 1-1-1 trichloroethane and tetrachloroethene residual saturation values of 15 to 40% in coarse Ottawa sand. Oostrom et al. (1999) give residual TCE saturation values in coarse, medium and fine sands as 22, 20 and 19%, respectively. If fingering had occurred then model resistivity, and consequently calculated residual DNAPL saturation levels, will represent average values for contaminated and uncontaminated material at the scale of a model cell; calculated residual saturations in this instance would therefore be lower than those determined from laboratory bulk samples.

6. SUMMARY AND CONCLUSIONS

EIT was used to monitor the migration of a fluorinated DNAPL through a porous polarizable medium within a laboratory column. Measured amplitude and phase data indicated rapid movement of DNAPL within the first hour of the experiment followed by a return to essentially static conditions. Measured amplitude and phase offsets after the initial dynamic phase indicated the presence of residual DNAPL within the flow path.

Differential resistivity images were successful in identifying DNAPL flow, and agreed well with the measured data. Resistivity anomalies consistent with the presence of residual DNAPL were still apparent in the late stages of the experiment. The size of the anomalies associated with the DNAPL flow indicated that some lateral spreading had occurred. Also the relatively modest increase in resistivity associated with the contaminated zone indicated that DNAPL had infiltrated only a limited proportion of the pores in the zone, and therefore fingering may well have occurred. Further experiments using dye-stained DNAPL are planned. These experiments would allow the extent and nature of flow to be visually assessed subsequent to electrical data collection, and would also include destructive sampling to determine residual saturation of DNAPL (Poulsen and Kueper,

1992). Comparisons between these data and the resistivity, phase and residual saturation models could then be made, thereby allowing the resolution of the EIT technique to be more robustly examined.

The differential phase images were less successful in delineating DNAPL flow, despite a significant phase shift identified in measured data associated with DNAPL contaminated material. Anomalies coinciding with the DNAPL were only apparent in the initial stages of the experiment, during which time DNAPL flow through the plane of electrodes was at a maximum. The differential phase images were of a relatively poor quality and were characterised by heterogeneous and variable phase angle distributions, seemingly unrelated to the DNAPL flow.

Resistivity data from individual model cells were used to estimate DNAPL saturation levels within the column. Residual saturation levels of up to 12% were calculated within the DNAPL flow path at the end of the experiment. These levels may be an underestimate of the true residual saturations at an inter-granular level, and instead probably represent an average value from uncontaminated material and DNAPL fingers within the flow path identified in the EIT images.

This study illustrates the potential value of EIT, and in particularly resistivity imaging, for the non-invasive monitoring of hydraulic experiments involving DNAPL invasion in laboratory conditions. Improvements in EIT monitoring of hydraulic experiments are likely to be achieved with the development of more rapid data acquisition systems, which will reduce errors due to DNAPL movement during data collection, and the use of data collection and inversion methodologies which fully account for the 3D nature of such experiments.

ACKNOWLEDGEMENTS

Funding for this research was provided by the joint EPSRC/NERC URGENT Programme (Grant No. GR/M34010) and the British Geological Survey. The work was jointly undertaken in conjunction with the University of Birmingham (co-investigator). This paper is published with

permission of the Executive Director of the British Geological Survey (NERC) and the University. The authors thank Gary Wealthall and Oliver Kuras, of the British Geological Survey, for their invaluable advice and assistance. We also wish to thank Gavin Harrold of the University of Greenwich for undertaking a number of the fluid property measurements used in this study.

LIST OF REFERENCES

Archie, G.E., 1942. The electrical resistivity log as an aid in determining some reservoir characteristics. Transactions of the AIME, 146: 54-62.

Bendat, J.S. and Piersol, A.G., 1971. Random Data: Analysis and measurement procedures. Wiley Interscience, New York.

Binley, A., Shaw, B. and HenryPoulter, S., 1996. Flow pathways in porous media: Electrical resistance tomography and dye staining image verification. Measurement Science & Technology, 7(3): 384-390.

Broholm, K., Feenstra, S. and Cherry, J.A., 1999. Solvent release into a sandy aquifer. 1. Overview of source distribution and dissolution behavior. Environmental Science & Technology, 33(5): 681-690.

Chambers, J., Ogilvy, R. and Meldrum, P., 1999. 3D resistivity imaging of buried oil- and tar contaminated waste deposits. European Journal of Environmental and Engineering Geophysics, 4: 3-14.

Chambers, J.E., 2001. The Application of 3D Electrical Tomography to the Investigation of Brownfield Sites. PhD Thesis, University of Sheffield, Sheffield.

Cho, J.S., 1996. Air sparging experiments on a two dimensional sand box with DNAPLs: multiphase investigation with electrical impedance tomography. In: L.N. Reddi (Editor), Non-Aqueous Phase Liquids (NAPLs) In Subsurface Environment: Assessment and Remediation. ASCE, New York, pp. 127-138.

Clavier, C., Heia, A. and Scala, C., 1976. Effect of pyrite on resistivity and other logging measurements. SPWLA Seventeenth annual logging symposium. Society of Professional Well Log Analysts. Houston, TX, United States, Denver, Colo., United States.

Coggon, J.H., 1971. Electromagnetic and electrical modelling by the finite element method. Geophysics, 36: 132-155.

Cohen, R.M. and Mercer, J.W., 1993. DNAPL Site Evaluation. C. K. Smoloy, Boca Raton, Florida,

384 pp.

Daily, W. and Ramirez, A., 1995. Electrical resistance tomography during in-situ trichloroethylene remediation at the Savannah River Site. Journal of Applied Geophysics, 33(4): 239-249.

Daily, W., Ramirez, A. and Johnson, R., 1998. Electrical impedance tomography of a perchloroethelyne release. Journal of Environmental and Engineering Geophysics, 2(3): 189-201.

Daily, W., Ramirez, A., Labrecque, D. and Nitao, J., 1992. Electrical-resistivity tomography of vadose water-movement. Water Resources Research, 28(5): 1429-1442.

Daily, W., Ramirez, A., Newmark, R. and George, V., 2000. Imaging UXO using electrical impedance tomography. Journal of Environmental and Engineering Geophysics, 5(4): 11-23.

deGroot-Hedlin, C. and Constable, S., 1990. Occam's inversion to generate smooth, two-dimensional models from magnetotelluric data. Geophysics, 55(12): 1613-1624.

Ellis, R.G. and Oldenburg, D.W., 1994. Applied geophysical inversion. Geophysical Journal International, 116(1): 5-11.

Feenstra, S. and Cherry, J.A., 1996. Diagnosis and Assessment of DNAPL Sites. In: J.F. Pankow and J.A. Cherry (Editors), Dense Chlorinated Solvents and other DNAPLs in Groundwater. Waterloo Press, Portland, Oregon, pp. 395-473.

Gavaskar, A., Rosansky, S., Naber, S., Gupta, N., Sass, B., Sminchak, J., DeVane, M. P., and Holdsworth, T., 2000. DNAPL delineation with soil and groundwater sampling. In: Wickramanayake, G. B., Gavaskar, A. R. and Gupta, N. (Eds.), Treating Dense Nonaqueous-Phase Liquids (DNAPLs): Remediation of Chlorinated and Recalcitrant Compounds. Battelle Press, Columbus, pp. 49-58.

George, A. and Liu, J.W.-H., 1981. Computer Solution of Large Sparse Positive Definite Systems. Prentice- Hall Inc., Englewood Cliffs, New Jersey.

Hagrey, S.A.al, Ismaeil, A., Meissner, R., Rabbel, W., 2003. Hydro- and bio-geophysical studies at an Olive farm, Canosa, Italy. EGS - AGU - EUG Joint Assembly, Nice, France, 6-11

April.

Harrold, G., Gooddy, D.C., Lerner, D.N. and Leharne, S.A., 2001. Wettability changes in trichloroethylene-contaminated sandstone. Environmental Science & Technology, 35(7): 1504-1510.

Hearst, J.R., Nelson, P.H. and Paillet, F.L., 1999. Well Logging For Physical Properties. Second Edition. John Wiley & Sons, Ltd, Chichester, 483 pp.

Imhoff, P.T., Arthur, M.H. and Miller, C.T., 1998. Complete dissolution of trichloroethylene in saturated porous media. Environmental Science & Technology, 32(16): 2417-2424.

ITRC, 2000. Dense Non-Aqueous Phase Liquids (DNAPLs): Review of Emerging Characterization and Remediation Technologies, Interstate Technology and Regulatory Cooperation (ITRC) Work Group, DNAPLs/Chemical Oxidation Work Team.

Johnson, R.L. and Pankow, J.F., 1992. Dissolution of Dense Chlorinated Solvents into Groundwater .2. Source Functions for Pools of Solvent. Environmental Science & Technology, 26(5): 896-901.

Kemna, A., Binley, A., Ramirez, A. and Daily, W., 2000. Complex resistivity tomography for environmental applications. Chemical Engineering Journal, 77(1-2): 11-18.

Kueper, B.H. and McWhorter, D.B., 1991. The Behavior of Dense, Nonaqueous Phase Liquids in Fractured Clay and Rock. Ground Water, 29(5): 716-728.

Kueper, B.H., Abbott, W. and Farquhar, G., 1989. Experimental observations of multiphase flow in heterogeneous porous media. Journal of Contaminant Hydrology, 5(1): 83-95.

Lines, L.R. and Treitel, S., 1984. Tutorial - a review of least-squares inversion and its application to geophysical problems. Geophysical Prospecting, 32(2): 159-186.

Loke, M.H. and Dahlin, T., 2002. A comparison of the Gauss-Newton and quasi-Newton methods in resistivity imaging inversion. Journal of Applied Geophysics, 49(3): 149-162.

Loke, M.H. and Lane, J.W., 2002. The use of constraints in 2D and 3D resistivity modelling,

Proceedings of the 8th general annual meeting of the European Section of the Environmental and Engineering Society, Aveiro, Portugal.

Lucius, J.E., Olhoeft, G.R., Hill, P.L. and Duke, S.K., 1992. Properties and hazards of 108 selected substances - 1992 edition. Open-File Report 92-527, U. S. Geological Survey.

Marshall, D.J. and Madden, T.R., 1959. Induced polarization, a study of its causes. Geophysics, 24: 790-816.

Mercer, J.W. and Cohen, R.M., 1990. A review of immiscible fluids in the subsurface: properties, models, characterisation and remediation. Journal of Contaminant Hydrology, 6: 107-163.

Nelson, P.H. and Van Voorhis, G.D., 1973. Letter to the editor regarding the paper "Complex resistivity spectra of porphyry copper mineralization". Geophysics, 38: 984.

Newmark, R.L., Daily, W.D., Kyle, K.R. and Ramirez, A.L., 1998. Monitoring DNAPL pumping using integrated geophysical techniques. Journal of Environmental and Engineering Geophysics, 3(1): 7-13.

Oldenburg, D.W. and Li, Y.G., 1994. Inversion of induced polarization data. Geophysics, 59(9): 1327-1341.

Olhoeft, G.R., 1985. Low-frequency electrical-properties. Geophysics, 50(12): 2492-2503.

Oostrom, M., Hofstee, C., Walker, R.C. and Dane, J.H., 1999. Movement and remediation of trichloroethylene in a saturated heterogeneous porous medium 1. Spill behavior and initial dissolution. Journal of Contaminant Hydrology, 37(1-2): 159-178.

Pankow, J.F. and Cherry, J.A., 1996. Dense Chlorinated Solvents and other DNAPLs in Groundwater. Waterloo Press, Portland, Oregon, 522 pp.

Pankow, J.F., Feenstra, S., Cherry, J.A. and Ryan, M.C., 1996. Dense Chlorinated Solvents in Groundwater: Background and History of the Problem. In: J.F. Pankow and J.A. Cherry (Editors), Dense Chlorinated Solvents and Other DNAPLs in Groundwater. Waterloo Press, Portland, Oregon, pp. 1-52.

Poulsen, M.M. and Kueper, B.H., 1992. A Field Experiment to Study the Behavior of Tetrachloroethylene in Unsaturated Porous-Media. Environmental Science & Technology, 26(5): 889-895.

Ramirez, A., Daily, W., Binley, A. and LaBrecque, D., 1999. Electrical impedance tomography of known targets. Journal of Environmental and Engineering Geophysics, 4(1): 11-26.

Reynolds, J.M., 1997. An Introduction to Applied and Environmental Geophysics. John Wiley & Sons, Chichester, 796 pp.

Rivett, M.O., Lerner, D.N. and Lloyd, J.W., 1990. Chlorinated Solvents in UK Aquifers. Journal of the Institution of Water and Environmental Management, 4(3): 242-250.

Sasaki, Y., 1989. Two-dimensional joint inversion of magnetotelluric and dipole- dipole resistivity data. Geophysics, 54(2): 254-262.

Schima, S., LaBrecque, D.J. and Lundegard, P.D., 1996. Monitoring air sparging using resistivity tomography. Ground Water Monitoring and Remediation, 16(2): 131-138.

Schwille, F., 1988. Dense Chlorinated Solvents in Porous and Fractured Media. Lewis Publishers, Inc., Michigan, USA, 146 pp.

Silvester, P.P. and Ferrari, R.L., 1990. Finite Elements for Electrical Engineers. Cambridge University Press, Cambridge, 344 pp.

Slater, L., Binley, A.M., Daily, W. and Johnson, R., 2000. Cross-hole electrical imaging of a controlled saline tracer injection. Journal of Applied Geophysics, 44(2-3): 85-102.

Sumner, J.S., 1976. Principles of Induced Polarization For Geophysical Exploration. Developments in Economic Geology, 5. Elsevier Scientific Publishing Company, Amsterdam, 277 pp.

Trantham, H. and Durnford, D., 1999. Stochastic aggregation model (SAM) for DNAPL-water displacement in porous media. Journal of Contaminant Hydrology, 36(3-4): 377-400.

Vanhala, H., 1997. Mapping oil-contaminated sand and till with the spectral induced polarization (SIP) method. Geophysical Prospecting, 45(2): 303-326.

Van Voorhis, G.D., Nelson, P.H. and L, D.T., 1973. Complex resistivity spectra of porphyry copper

mineralization. Geophysics, 38(1): 49-60.

Weidelt, P. and Weller, A., 1997. Computation of geoelectrical configuration factors for cylindrical core samples. Scientific Drilling, 6: 24-27.

Weller, A., Seichter, M. and Kampke, A., 1996a. Induced-polarization modelling using complex electrical conductivities. Geophysical Journal International, 127(2): 387-398.

Weller, A., Gruhne, M., Seichter, M. and Borner, F. D., 1996b. Monitoring hydraulic experiments by complex conductivity tomography. European Journal of Environmental and Engineering Geophysics, 1: 209-228.

FIGURE CAPTIONS

Figure 1. Schematic diagram of laboratory column, including porous media distribution, in (a) section and (b) plan view. The PVC column and carbon electrodes are shown in grey and black, respectively.

Figure 2. (a) SIP256b system architecture showing current electrodes switched to remote units 5 and 6. (b) Measurement protocol for a scan that includes all dipole-dipole positions for which each dipole length is equal to one unit electrode separation.

Figure 3. (a) Example of the dipole-dipole array on a cylindrical surface (where dipole length is denoted by ‘a’ and dipole separation factor by ‘n’), including model elements and an exploded view of the shape and locations of the nodes for an isoparametric quadrilateral element with 8 nodes, and (b) an example of an inverted model generated using this mesh geometry from a test with a known target.

Figure 4. Base line scans collected prior to DNAPL release showing model resistivity and phase angle.

Figure 5. Measured amplitude (resistance) and phase breakthrough curves, collected using remote units 7 (C1), 8 (C2), 10 (P1) and 11 (P2). Error bars show SIP256b calculated error.

Figure 6. Differential resistivity and phase time-lapse images collected at t = 4.5, 13.5, 22.5, 31.5, 49.5 and 481.5 min. The horizontal position of the DNAPL surface release point is shown as a circle.

Figure 7. Breakthrough curves of model resistivity and phase angle for cells 38 and 142.

Figure 8. Contour plot showing calculated residual DNAPL saturation at t = 481.5 min.

TABLES

Physical Properties	HFE-7200	Trichloroethene
Density (kg/m^3)	1430 [a]	1460 [b]
Dynamic Viscosity (Pa.s)	0.00061 [a]	0.00057 [b]
Interfacial Liquid Tension (N/m)	0.0382 [c]	0.0345 [b]
Contact Angle, Sessile (degree) - quartz	30 ±1 [d]	20 ±5 [e]
Solubility in Water @ 25^{o}C(mg/L)	<20 [a]	1100 [f]
Resistivity (Ωm)	10^6 [a]	10^6 [f]

Data from [a] 3M Product Data Sheet, [b] Oostrom et al. (1999), [c] Centre for Contaminated Land Remediation (CCLR), University of Greenwich, UK, measured using Krüss DSA 10, [d] CCLR, [e] Harrold et al. (2001) and [f] Lucius et al. (1992).

Table 1. Fluid properties.

Dipole-dipole array 'n' value	Geometric factor (m)	Number of measurements	Average apparent resistivity (Ωm)	Standard deviation (Ωm)
1	1.4165	12	17.38	0.47
2	4.8004	12	16.61	0.22
3	10.077	12	16.86	0.28
4	15.265	12	17.23	0.21
5	17.479	6	17.37	0.27

Table 2. The geometric factors for the dipole-dipole array for a cylindrical geometry. The apparent resistivity values were produced from a test with tap water.

Pore Fluid (%)		Resistivity (Ωm)
Water	NAPL	
100	0	54
95	5	60
90	10	67
80	20	84
60	40	150

Table 3. Clean porous media resistivity as a function of DNAPL saturation.

Figure 1

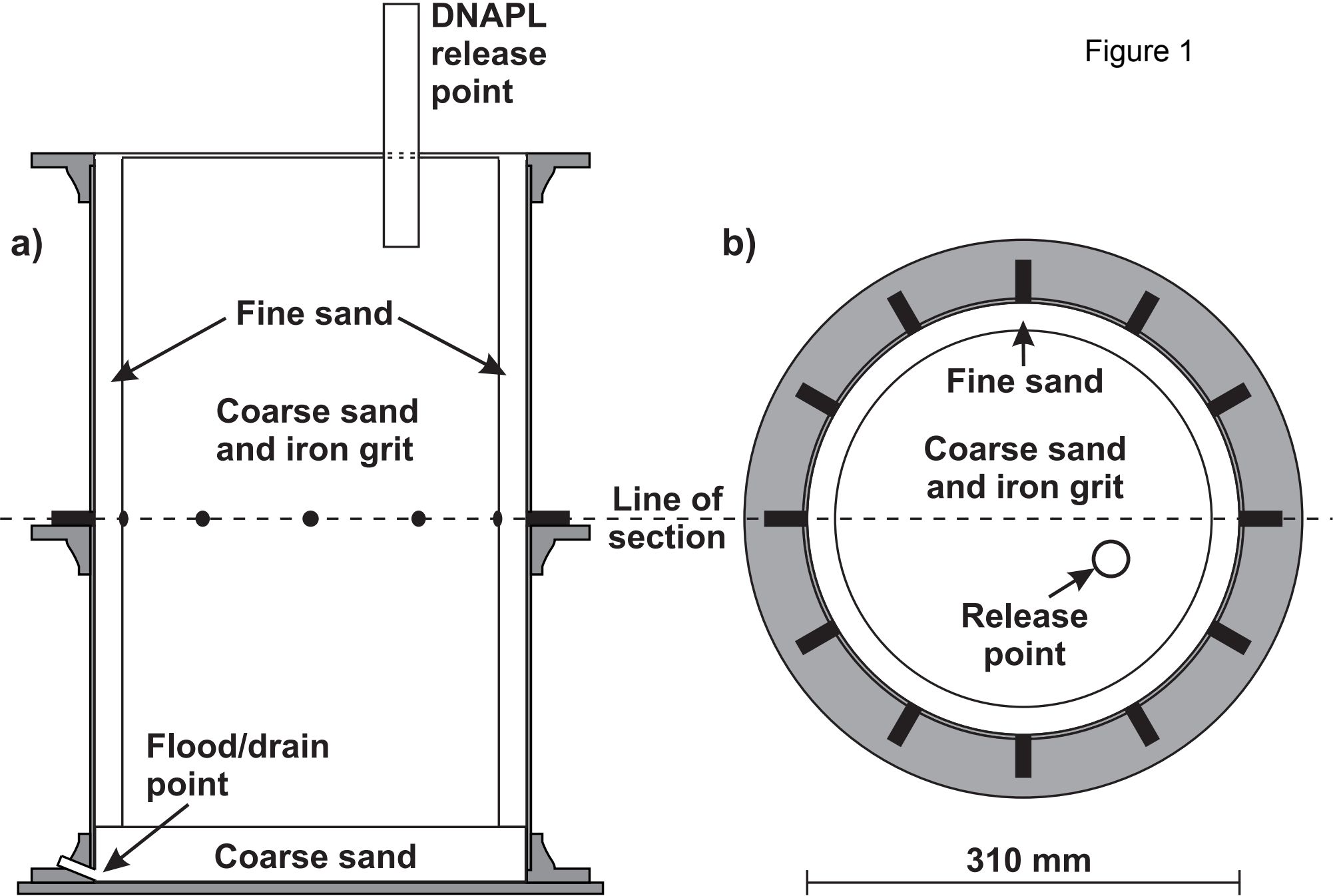
DNAPL release point
a)
Fine sand
Coarse sand and iron grit
Line of section
Flood/drain point
Coarse sand
b)
Fine sand
Coarse sand and iron grit
Release point
310 mm

a)

Figure 2

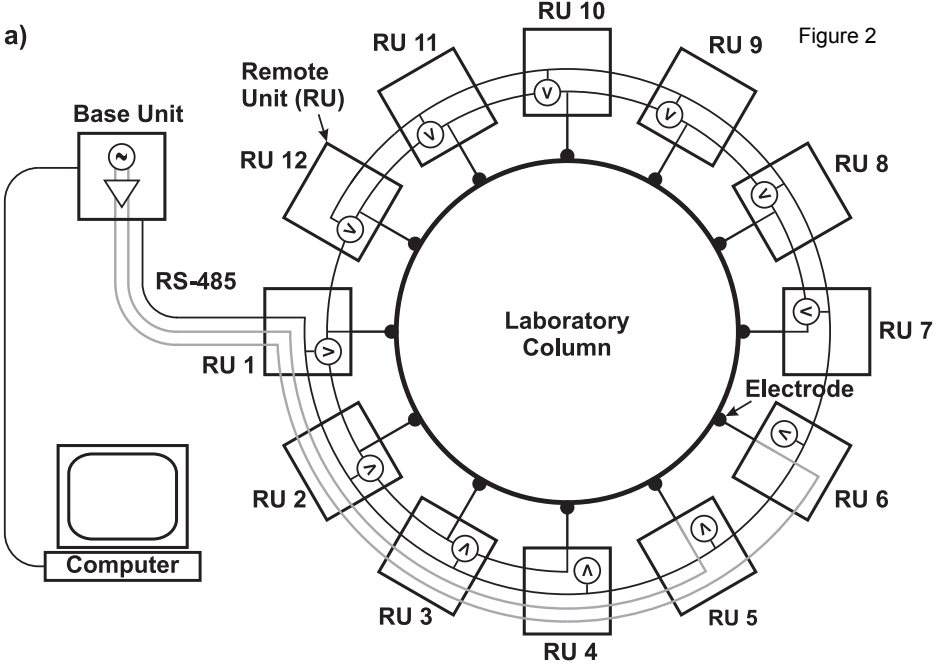

b)

Measurement	RU1	RU2	RU3	RU4	RU5	RU6	RU7	RU8	RU9	RU10	RU11	RU12
1	***C1***	***C2***	*P1*	*P2/P1*	*P2/P1*	*P2/P1*	*P2/P1*	*P2/P1*	*P2/P1*	*P2/P1*	*P2/P1*	*P2*
2	*P2*	***C1***	***C2***	*P1*	*P2/P1*	*P2/P1*	*P2/P1*	*P2/P1*	*P2/P1*	*P2/P1*	*P2/P1*	*P2/P2*
3	*P2/P1*	*P2*	***C1***	***C2***	*P1*	*P2/P1*	*P2/P1*	*P2/P1*	*P2/P1*	*P2/P1*	*P2/P1*	*P2/P1*
4	*P2/P1*	*P2/P1*	*P2*	***C1***	***C2***	*P1*	*P2/P1*	*P2/P1*	*P2/P1*	*P2/P1*	*P2/P1*	*P2/P1*
5	*P2/P1*	*P2/P1*	*P2/P1*	*P2*	***C1***	***C2***	*P1*	*P2/P1*	*P2/P1*	*P2/P1*	*P2/P1*	*P2/P1*
6	*P2/P1*	*P2/P1*	*P2/P1*	*P2/P1*	*P2*	***C1***	***C2***	*P1*	*P2/P1*	*P2/P1*	*P2/P1*	*P2/P1*
7	*P2/P1*	*P2/P1*	*P2/P1*	*P2/P1*	*P2/P1*	*P2*	***C1***	***C2***	*P1*	*P2/P1*	*P2/P1*	*P2/P1*
8	*P2/P1*	*P2/P1*	*P2/P1*	*P2/P1*	*P2/P1*	*P2/P1*	*P2*	***C1***	***C2***	*P1*	*P2/P1*	*P2/P1*
9	*P2/P1*	*P2/P1*	*P2/P1*	*P2/P1*	*P2/P1*	*P2/P1*	*P2/P1*	*P2*	***C1***	***C2***	*P1*	*P2/P1*
10	*P2/P1*	*P2/P1*	*P2/P1*	*P2/P1*	*P2/P1*	*P2/P1*	*P2/P1*	*P2/P1*	*P2*	***C1***	***C2***	*P1*
11	*P2/P1*	*P2/P1*	*P2/P1*	*P2/P1*	*P2/P1*	*P2/P1*	*P2/P1*	*P2/P1*	*P2/P1*	*P2*	***C1***	***C2***
12	***C2***	*P1*	*P2/P1*	*P2/P1*	*P2/P1*	*P2/P1*	*P2/P1*	*P2/P1*	*P2/P1*	*P2/P1*	*P2*	***C1***

Figure 3

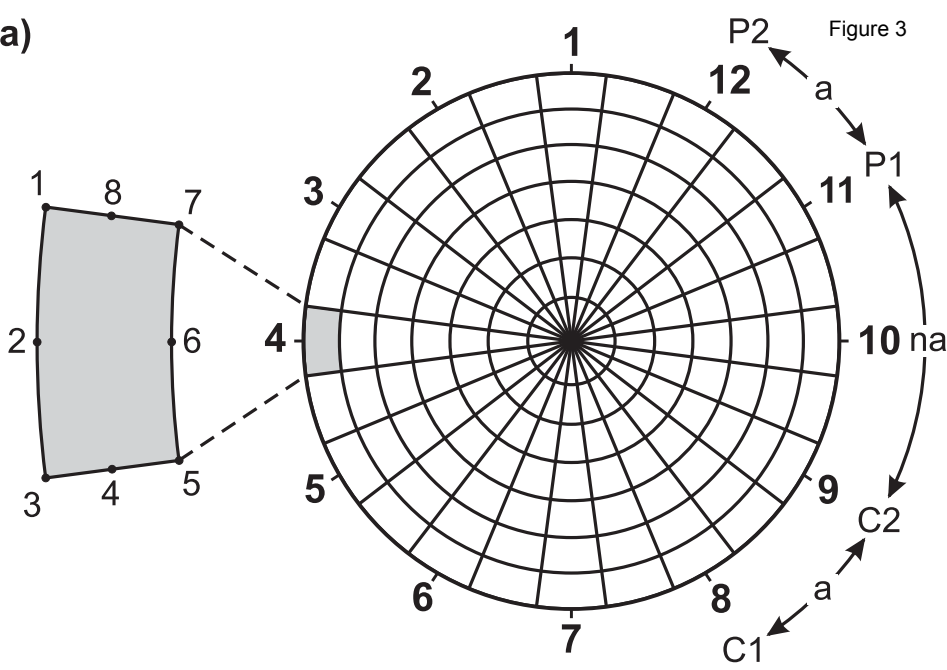
a)
1
2
3
4
5
6
7
8
P2
a
P1
na
C2
a
C1
1
8
7
2
6
3
4
5

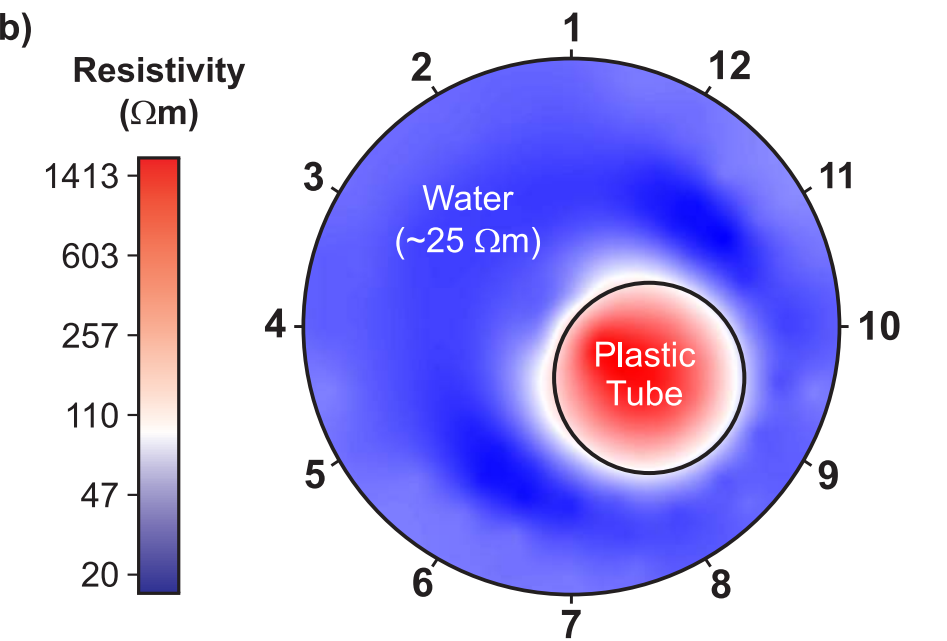
b)
Resistivity
(Ωm)
1413
603
257
110
47
20
Water
(~25 Ωm)
Plastic
Tube
1
2
3
4
5
6
7
8
9
10
11
12

Figure 4

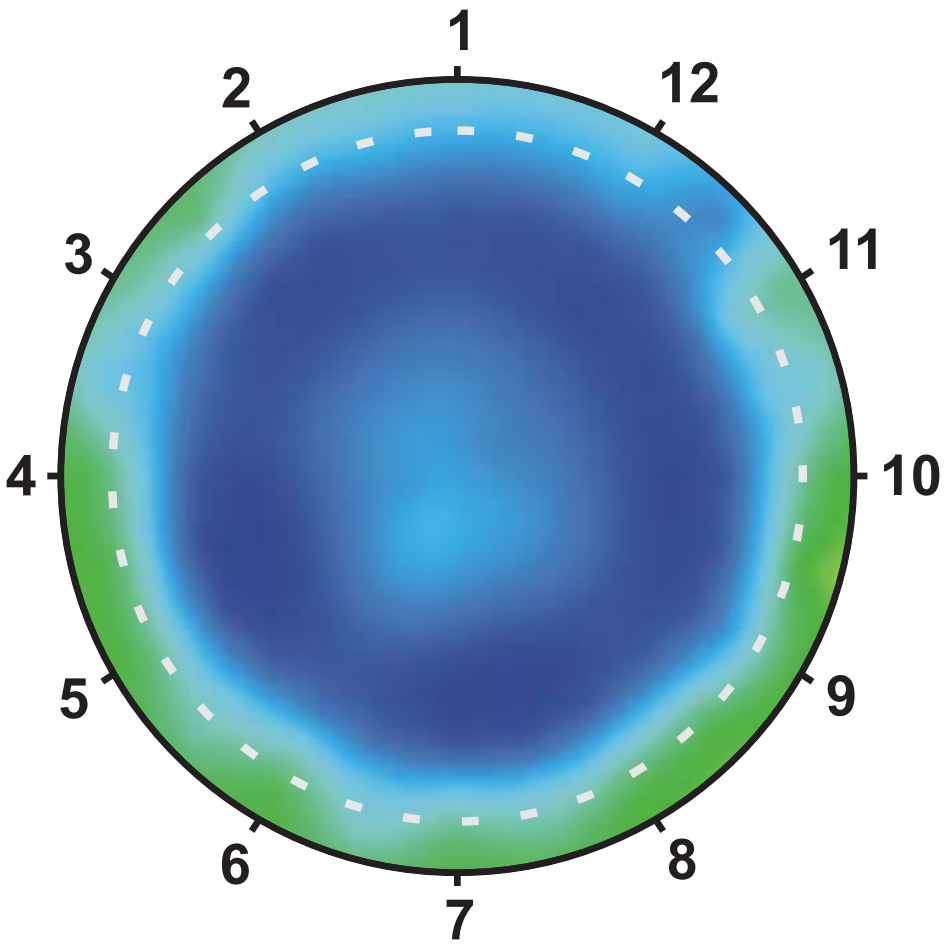

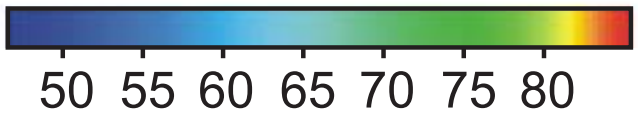

Resistivity (Ωm)

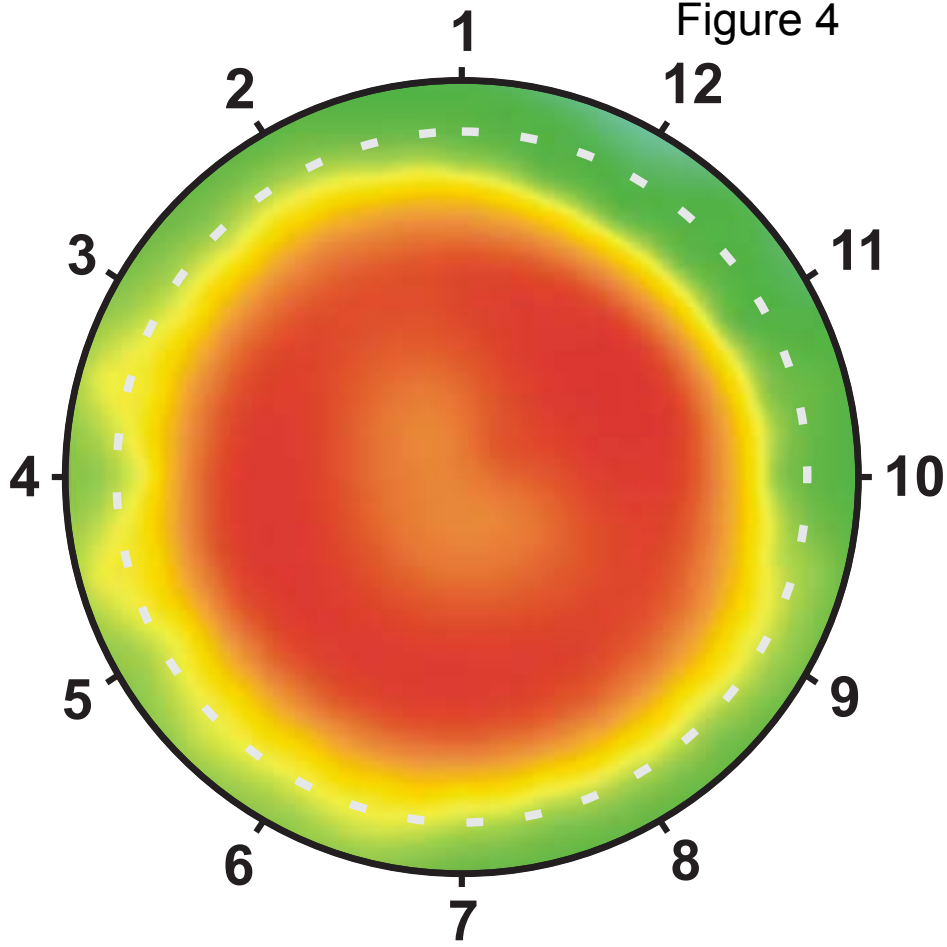

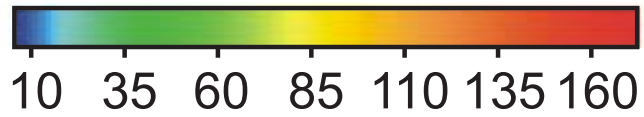

Phase Angle (mrad)

Figure 5

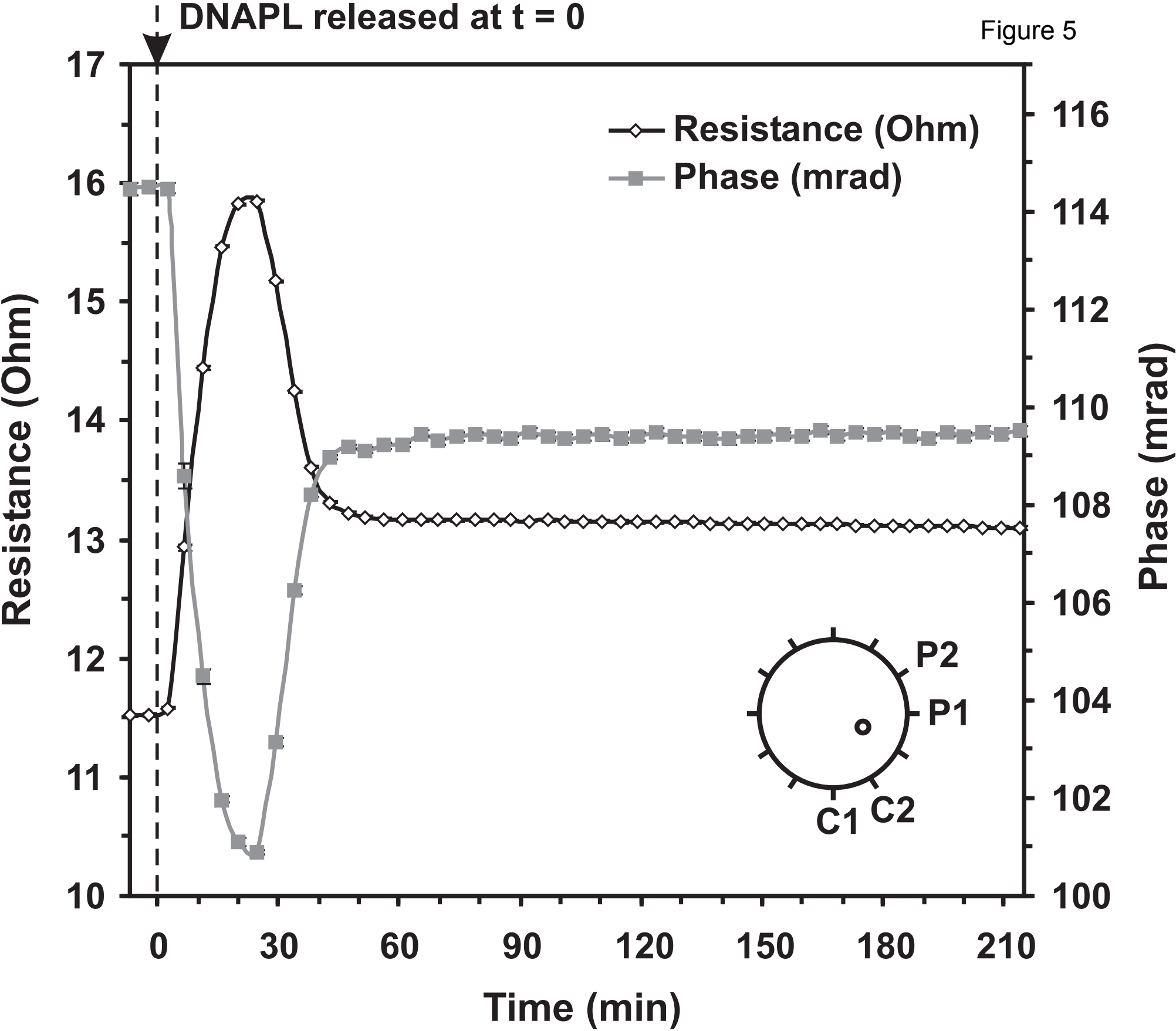
DNAPL released at t = 0
Resistance (Ohm)
Phase (mrad)
Resistance (Ohm)
Phase (mrad)
Time (min)
17
16
15
14
13
12
11
10
116
114
112
110
108
106
104
102
100
0
30
60
90
120
150
180
210
P2
P1
C1
C2

Figure 6

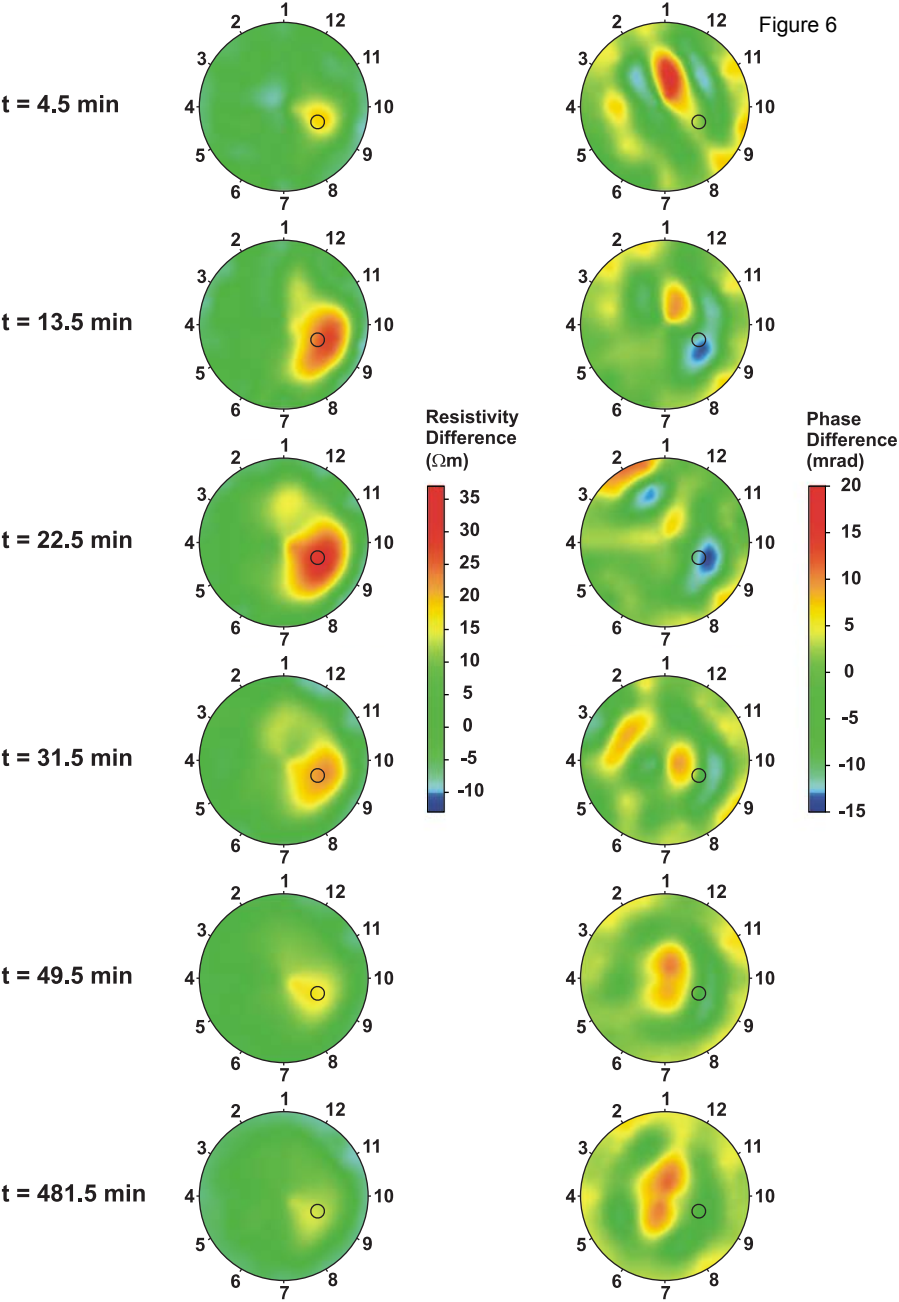
t = 4.5 min
t = 13.5 min
t = 22.5 min
t = 31.5 min
t = 49.5 min
t = 481.5 min
Resistivity Difference (Ωm)
35
30
25
20
15
10
5
0
-5
-10
Phase Difference (mrad)
20
15
10
5
0
-5
-10
-15
1
2
3
4
5
6
7
8
9
10
11
12

Figure 7

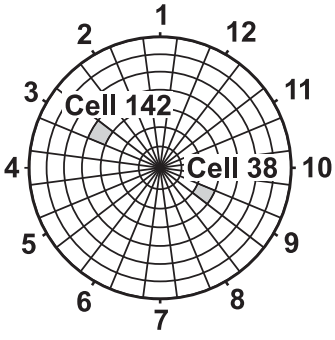

Finite element mesh geometry showing cell locations

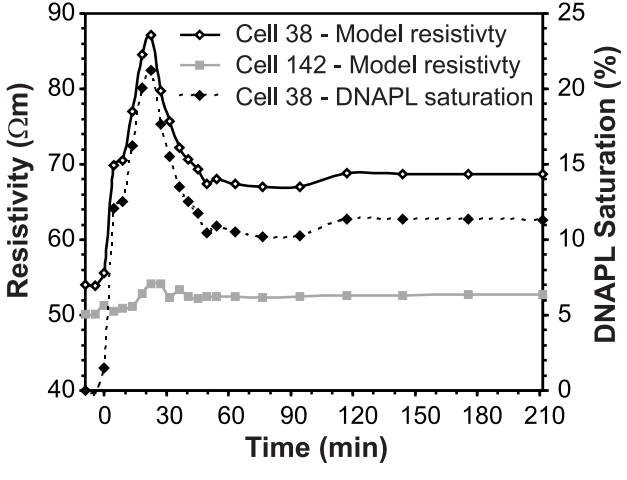

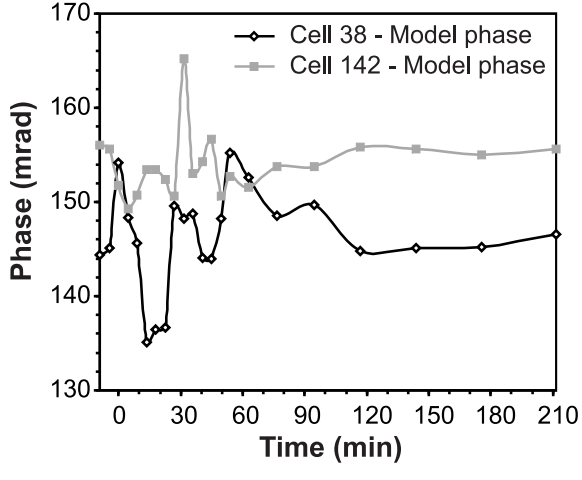

Figure 8